Opto-Electronic Science

CN 51–1800/O4 ISSN 2097–0382 (Print) ISSN 2097–4000 (Online)

Broadband ultrasound generator over fiber-optic tip for *in vivo* emotional stress modulation

Jiapu Li, Xinghua Liu, Zhuohua Xiao, Shengjiang Yang, Zhanfei Li, Xin Gui, Meng Shen, He Jiang, Xuelei Fu, Yiming Wang, Song Gong, Tuan Guo and Zhengying Li

Citation: Li JP, Liu XH, Xiao ZH, et al. Broadband ultrasound generator over fiber-optic tip for *in vivo* emotional stress modulation. *Opto-Electron Sci* **4**, 240034 (2025).

https://doi.org/10.29026/oes.2025.240034

Received: 12 December 2024; Accepted: 10 February 2025; Published online: 18 April 2025

Related articles

Direct detection with an optimal transfer function: toward the electrical spectral efficiency of coherent homodyne detection

Xingfeng Li, Jingchi Li, Xiong Ni, Hudi Liu, Qunbi Zhuge, Haoshuo Chen, William Shieh, Yikai Su

Opto-Electronic Science 2025 **4**, 240020 doi: 10.29026/oes.2025.240020

Smart photonic wristband for pulse wave monitoring

Renfei Kuang, Zhuo Wang, Lin Ma, Heng Wang, Qingming Chen, Arnaldo Leal Junior, Santosh Kumar, Xiaoli Li, Carlos Marques, Rui Min

Opto-Electronic Science 2024 **3**, 240009 doi: 10.29026/oes.2024.240009

Three-dimensional multichannel waveguide grating filters

Si-Yu Yin, Qi Guo, Shan-Ren Liu, Ju-Wei He, Yong-Sen Yu, Zhen-Nan Tian, Qi-Dai Chen

Opto-Electronic Science 2024 **3**, 240003 doi: 10.29026/oes.2024.240003

High-resolution tumor marker detection based on microwave photonics demodulated dual wavelength fiber laser sensor

Jie Hu, Weihao Lin, Liyang Shao, Chenlong Xue, Fang Zhao, Dongrui Xiao, Yang Ran, Yue Meng, Panpan He, Zhiguang Yu, Jinna Chen, Perry Ping Shum

Opto-Electronic Advances 2024 **7**, 240105 doi: 10.29026/oea.2024.240105

Opto-Electronic Science

Article

xxxx 2025, Vol. x, No.

DOI: 10.29026/oes.2025.240034 CSTR: 32246.14.oes.2025.240034

Broadband ultrasound generator over fiber-optic tip for *in vivo* emotional stress modulation

Jiapu Li[2†], Xinghua Liu[1,3†*], Zhuohua Xiao[2†], Shengjiang Yang[2], Zhanfei Li[1,3], Xin Gui[4], Meng Shen[5], He Jiang[2], Xuelei Fu[2], Yiming Wang[2], Song Gong[1,3], Tuan Guo[6] and Zhengying Li[2,4*]

Ultrasonic neuromodulation has gained recognition as a promising therapeutic approach. A miniature transducer capable of generating suitable-strength and broadband ultrasound is of great significance for achieving high spatial precision ultrasonic neural stimulation. However, the ultrasound transducer with the above integrated is yet to be challenged. Here, we developed a fiber-optic photoacoustic emitter (FPE) with a diameter of 200 μm, featuring controllable sound intensity and a broadband response (−6 dB bandwidth: 162%). The device integrates MXene ($Ti_3C_2T_x$), known for its exceptional photothermal properties, and polydimethylsiloxane, which offers a high thermal expansion coefficient. This FPE, exhibiting high spatial precision (lateral: 163.3 μm, axial: 207 μm), is capable of selectively activating neurons in targeted regions. Using the TetTagging method to selectively express a cfos-promoter-inducible mCHERRY gene within the medial prefrontal cortex (mPFC), we found that photoacoustic stimulation significantly and temporarily activated the neurons. In vivo fiber photometry demonstrated that photoacoustic stimulation induced substantial calcium transients in mPFC neurons. Furthermore, we confirmed that photoacoustic stimulation of the mPFC using FPE markedly alleviates acute social defeat stress-induced emotional stress in mice. This work demonstrates the potential of FPEs for clinical applications, with a particular focus on modulating neural activity to regulate emotions.

Keywords: fiber-optic; photoacoustic emitter; ultrasonic nerve stimulation; high spatial precision

Li JP, Liu XH, Xiao ZH et al. Broadband ultrasound generator over fiber-optic tip for *in vivo* emotional stress modulation. *Opto-Electron Sci* **x**, 240034 (2025).

[1]Division of Trauma Surgery, Emergency Surgery & Surgical Critical, Tongji Trauma Center, Tongji Hospital, Tongji Medical College, Huazhong University of Science and Technology, Wuhan 430030, China; [2]School of Information Engineering, Wuhan University of Technology, Wuhan 430070, China; [3]Department of Emergency and Critical Care Medicine, Tongji Hospital, Tongji Medical College, Huazhong University of Science and Technology, Wuhan 430030, China; [4]National Engineering Research Center of Fiber Optic Sensing Technology and Networks, State Key Laboratory of Advanced Technology for Materials Synthesis and Processing, Wuhan University of Technology, Wuhan 430070, China; [5]Hubei Key Laboratory of Micro-Nanoelectronic Materials and Devices, Hubei Collaborative Innovation Center for Advanced Organic Chemical Materials, Ministry of Education Key Laboratory of Green Preparation and Application for Functional Materials, and School of Microelectronics, Hubei University, Wuhan 430062, China; [6]Institute of Photonics Technology, Jinan University, Guangzhou 510632, China.

[†]These authors contributed equally to this work.

*Correspondence: ZY Li, E-mail: zhyli@whut.edu.cn; XH Liu, E-mail: hualiu@tjh.tjmu.edu.cn

Received: 12 December 2024; Accepted: 10 February 2025; Published online: 18 April 2025

Introduction

Ultrasound neuromodulation, as a technique for controlling neural activity, has garnered increasing attention in recent years[1–3]. It has been proven that ultrasound can treat and improve neurological disorders by modulate synaptic activity, trigger action potentials, and alter neurotransmitter release[4–6]. However, when transmitted externally, ultrasound encounters significant scattering and reflection due to the skull's high acoustic impedance, potentially leading to off-target stimulation and even traumatic, irreversible brain injury[7–9]. Implantable devices enable electrical and chemical modulation of the brain, significantly advancing the precise treatment of neurological and psychiatric disorders[7,10]. Nonetheless, developing a scalable implant system without electrochemically active elements that can locally reversible modulate neurons in subcortical brain regions remains a significant challenge in treating brain nervous system diseases[7].

Fiber-optic photoacoustic neural stimulation, a novel technique leveraging optical fibers, offers a groundbreaking approach to modulating neural activity with high spatial precision and minimal invasiveness[3,11,12]. Studies have shown that fiber-optic photoacoustic stimulation can evoke precise and controlled neural responses, opening new avenues for treating neurological disorders like Parkinson's disease, epilepsy, and chronic pain[5,11,12]. Compared to conventional electrical stimulation, fiber-optic photoacoustic stimulation provides several advantages: it eliminates the need for direct electrode contact with neural tissue, reduces the risk of tissue damage or immune response, and allows for more precise targeting of neural circuits[5,12,13]. This approach involves positioning miniature fiber-optic photoacoustic emitter (FPE) adjacent to target neural structures, which can include deep brain regions or peripheral nerve bundles. The FPE operates on the principle of the photoacoustic effect. A pulse laser is transmitted through fiber-optic to emitter, where the light-absorption material undergoes photothermal conversion. This process generates heat, which is transmitted to the thermal expansion material to produce periodic thermal expansion and contraction, subsequently generating ultrasonic waves capable of activating nearby neurons[14–17]. This method not only provides the potential for chronic and long-term neuromodulation but also offers the flexibility of parameter adjustments to refine therapeutic outcomes. Furthermore, this technique is compatible with other optical methods, such as fiber photometry, enabling real-time monitoring and adjustment of stimulation patterns.

Emotional stress, a common form of tension in daily life, can disrupt the body's homeostasis[18]. Beyond affecting peripheral organ functionality, maladaptive and uncontrollable responses to emotional stress may contribute to central nervous system disorders such as anxiety, post-traumatic stress disorder (PTSD), epilepsy, and ischemic stroke[19–21]. Multiple brain regions in mammals are involved in coping with emotional stress, including the prefrontal cortex (PFC), amygdala, anterior insula, hippocampus, and striatum[22–24]. Human neuroimaging evidence suggests that the medial prefrontal cortex (mPFC) is a critical locus within the adaptive behavioral coping circuit, regulating anxious emotions[25,26]. Under emotional stress, the activation of the stress, immune, and oxidative systems can converge into a state of mutual activation, potentially leading to behavioral and biochemical changes, thus forming a vicious cycle[27]. For instance, patients with sleep disorders exhibit weaker working memory performance, accompanied by reduced activation and functional connectivity in the subregions of the prefrontal cortex[28]. Chronic social defeat stress (SDS) induces differences in PFC oscillations that underlie the emergence of social behavioral dysfunction associated with stress-induced impairments[29]. Does fiber-optic photoacoustic neural modulation of the mPFC have a protective effect against emotional stress? A miniature FPE featuring controllable ultrasonic intensity and broadband is of great significance for achieving high spatial precision reversible neural stimulation. However, the FPE with the above integration remains a challenge. Moreover, optimizing the delivery parameters to minimize off-target effects and to maintain consistent stimulation outcomes across different individuals is critical.

To address the aforementioned open question, we developed a diameter 200 μm miniature FPE, designed to stimulate medial prefrontal cortex neurons. This device is composed of $Ti_3C_2T_x$ and polydimethylsiloxane (PDMS). The FPE employs a pulse laser to modulate the photothermal temperature field of $Ti_3C_2T_x$, resulting in periodic thermal expansion and contraction of the surrounding PDMS, which generates ultrasonic waves (Fig. 1(a)). The assembled device simultaneously achieves controllable sound intensity, broadband (−6 dB bandwidth: 162%), and high spatial precision (lateral: 163.3 μm, axial: 207 μm), with all parameters representing

exceptional values for FPE systems (Fig. 1(b)). The FPE implantable ultrasound stimulator is electrochemically inactive, exhibits good biocompatibility, is non-genetic, and can locally reversible modulate neurons in subcortical brain regions. Furthermore, we confirmed that ultrasound stimulation of the mPFC can relieve acute SDS-induced emotional stress. We implanted two fiber-optic probes simultaneously into the mPFC of mice, one for ultrasound neurostimulation and the other for fiber photometry recording of neuronal excitability in the mPFC. Using GCaMP, a calcium indicator expressed in the mPFC, we can directly record the correlation between ultrasound neurostimulation and neuronal excitability through calcium signals (Fig. 1(c)). The functionalities demonstrated by our developed FPE stimulator offer a highly promising approach for neuromodulation therapies in the treatment of neurological and neuropsychiatric disorders.

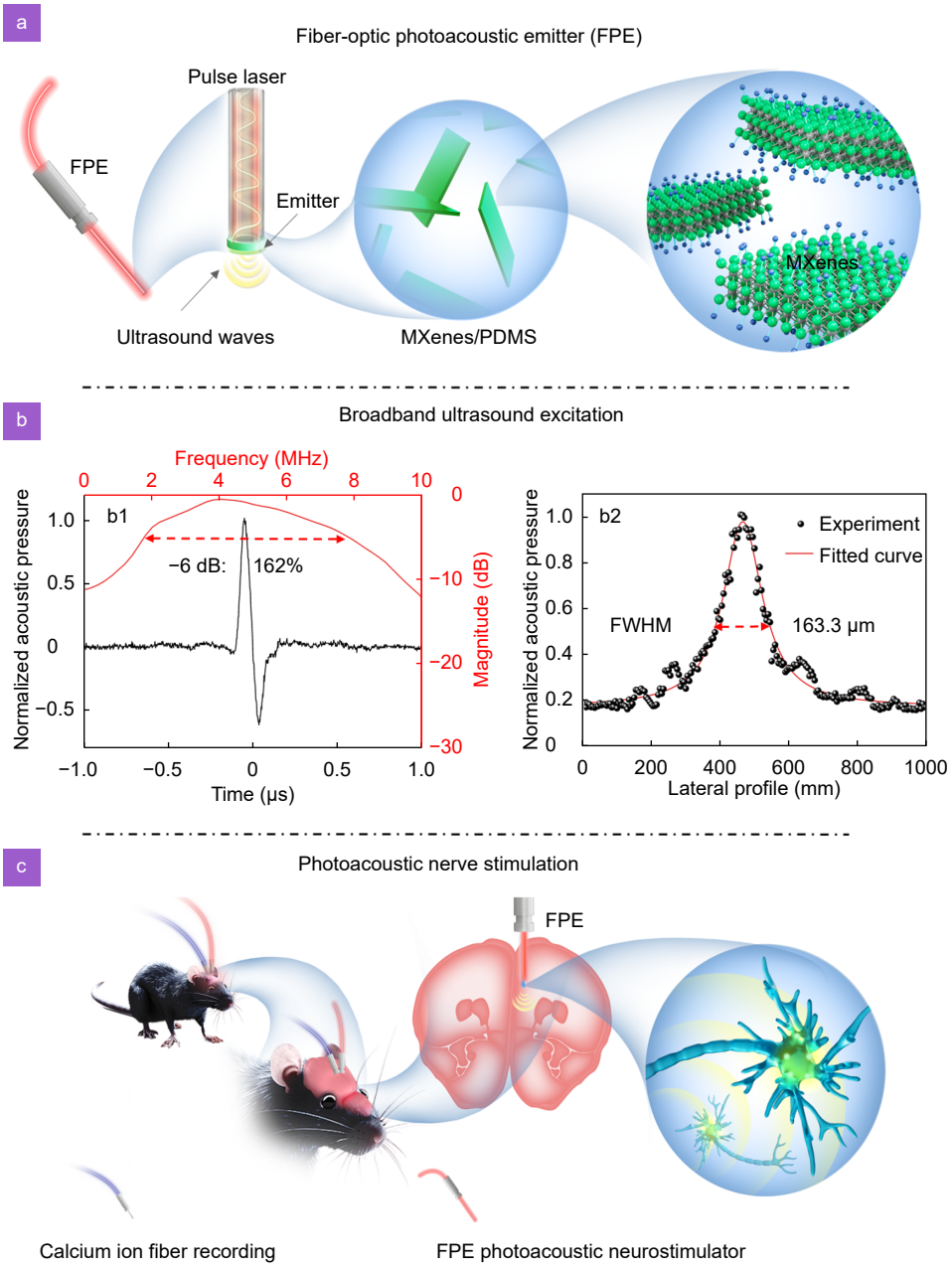

Fig. 1 | An implantable fiber-optic photoacoustic neurostimulator. (**a**) Schematic illustration of the FPE. (**b**) Broadband ultrasonic excitation of FPE, b1: time-domain and frequency-domain ultrasound response of FPE, b2: lateral distribution of FPE sound field. (**c**) Schematic diagram of FPE stimulation of medial prefrontal cortex in mice. Blue fiber-optic: fiber photometer for calcium ion recording; light red fiber-optic: FPE photoacoustic neurostimulator.

Experiments

Synthesis method of $Ti_3C_2T_x$ nanosheets

Hydrogen fluoride solution and delamination were employed to synthesize $Ti_3C_2T_x$ nanosheets from Ti_3AlC_2. Specifically, 1.0 g of Ti_3AlC_2 was gently added to 10 mL of hydrogen fluoride solution (40 wt.%) with magnetic stirring for 15 minutes to mitigate the exothermic reaction. Multiple layers of $Ti_3C_2T_x$ (the notation T_x refers to surface functional groups, such as –OH, –F, and =O, which are introduced during the synthesis) were obtained after hydrofluoric acid etching at room temperature for 48 hours, and fewer layers were achieved after ultrasonic treatment for 10 minutes. The mixture was then washed and centrifuged with deionized water several times until the pH of the supernatant was 6 or higher. Finally, the $Ti_3C_2T_x$ powders were vacuum dried at 80 °C for 12 hours.

Material characterization

The morphologies and microstructures of all the samples were analyzed using scanning electron microscopy (SEM, JSM-7800F, Japan) and transmission electron microscopy (TEM, JEOL-2100F, Japan). X-ray diffraction (XRD) was performed on a Bruker diffractometer (D8 Advance, Germany) with Cu K_α radiation, scanning 2θ from 3° to 70°. Ultraviolet-visible-NIR absorption spectra and diffuse reflectance absorption spectra were obtained using a UV-2700 spectrophotometer (Shimadzu, Japan). The lattice specific heat capacities of different materials were obtained using a DSC2500 differential scanning calorimeter (DSC2500, TA Instruments, USA). Thermogravimetric analysis was performed under an argon atmosphere using a Pyris1 TGA (PerkinElmer Instruments, USA), with a heating/cooling rate of 10 °C/min and a gas flow rate of 50 mL/min.

Preparation of fiber-optic photoacoustic emitter

Firstly, the $Ti_3C_2T_x$ (0.2 g), PDMS (1 g), curing agent (0.1 g) were added to prepare $Ti_3C_2T_x$/PDMS solution at a 5 mL beaker, and were then mixed for 10 min, followed by vacuum treatment for 30 min. Then, the fiber-optic (diameter: 200 μm) was inserted into the dip coating $Ti_3C_2T_x$/PDMS solution, held stationary for 30 s, and then withdrawn. After the $Ti_3C_2T_x$/PDMS composite was deposited at the end of the fiber-optic using multi-step dip coatings to prepare fiber-optic photoacoustic emitter. Finally, the $Ti_3C_2T_x$/PDMS composite was cured at 90 °C for keeping 10 min. The parameters of the pulse laser are as follows: energy: 0–10 mJ/pulse, pulse width: 10 ns, wavelength: 1064 nm, pulse repetition rate: 20 Hz, and the device model is Lapa-20 (Beamtech, China).

Animal experiment of fiber optic photoacoustic nerve stimulation

The ultrasound waves induce changes in neural potential, enabling the modulation of neural activity in mice. In animal experiments, wildtype C57BL/6J mice aged 6–8 weeks and CD1 mice aged 6–8 months were purchased from Huafukang Biotechnology Co., Ltd., Beijing, China. The mice were housed under stable conditions with a temperature of 22–25 °C and humidity of 50%±5%, maintained on a 12 hour light/dark cycle. All experimental procedures were conducted following the ARRIVE guidelines and were approved by the Experimental Animal Ethical Committee of Tongji Hospital, affiliated with Huazhong University of Science and Technology. Before the experiments, the mice were given at least 1 week to acclimatize to their new environment.

Results and discussion

Characterization of MXenes ($Ti_3C_2T_x$)

$Ti_3C_2T_x$ was synthesized by etching Al atoms from the ternary layered ceramic (Ti_3AlC_2) MAX phase using a multi-step hydrofluoric acid wet etching method, as depicted in Fig. 2(a). The morphology, microstructure, and chemical composition of the synthesized component are illustrated in Fig. 2(b, c) and detailed below the respective figures. Figure 2(b) shows the morphology and energy spectrum of the precursor MAX phase ceramic (Ti_3AlC_2), indicating homogeneous distribution of Ti, C, and Al elements. Figure 2(c) demonstrates that etching Ti_3AlC_2 results in the formation of $Ti_3C_2T_x$ with a distinct layered structure. The scanning electron microscope (SEM) element mapping analysis reveals homogeneous distribution of Ti and C across $Ti_3C_2T_x$. The transmission electron microscope (TEM) results show that Ti grains are closely anchored onto the nanosheets, ensuring intimate contact Fig. 2(c). The high resolution-TEM (HR-TEM) images display lattice fringes of 0.26 nm, corresponding to the d-spacing of the $(0\bar{1}10)$ crystal plane of $Ti_3C_2T_x$, indicating in situ formation of Ti Fig. 2(c). Additionally, HR-TEM images clearly show the restacking of Ti_3AlC_2 and $Ti_3C_2T_x$ layers, each approximately 0.8 nm thick, effectively preventing the aggregation of individual

$Ti_3C_2T_x$ nanosheets. This observation is consistent with previous results obtained using the molten salt method[30]. The observed structure differs significantly from the pristine Ti_3AlC_2 MAX phase precursor, as no Al atomic layer is present between the Ti_3C_2 layers, confirming the successful removal of Al through chemical etching. Figure 2(d) shows the X-ray diffraction (XRD) pattern results of $Ti_3C_2T_x$ produced after the MAX phase ceramics (Ti_3AlC_2) were etched by hydrofluoric acid. In the XRD pattern of $Ti_3C_2T_x$ (Fig. 2(d)), the (002) peak of the Ti_3AlC_2 MAX phase shifts from a 2θ angle of 9.52° to 8.95°. The calculated phonon spectra of $Ti_3C_2T_x$, obtained through first-principles calculations are shown in Fig. 2(e) and (Fig. S1). Theoretical calculation results confirm that $Ti_3C_2T_x$ is dynamically stable, as there are no negative frequencies in its phonon spectra. The value of the low phonon frequency, particularly the frequency of the acoustic modes, strongly depends on the titanium atoms. Acoustic phonons primarily affect the thermal properties of materials, thereby indirectly influencing their temperature changes. In addition, there is a frequency range where both acoustic and optical vibrational modes coexist. The absence of a gap between the acoustic and optical modes can lead to strong acoustic-optical scattering, significantly affecting the thermal property of the $Ti_3C_2T_x$. Figure 2(f) shows the thermogravimetric curve of $Ti_3C_2T_x$, indicating that $Ti_3C_2T_x$ has good thermal stability. Figure 2(g) demonstrates that $Ti_3C_2T_x$ has a low lattice specific heat capacity at room temperature (25 °C), allowing for significant temperature changes through photothermal conversion. Figure 2(h) demonstrates that $Ti_3C_2T_x$ exhibits exceptional light absorption properties at a wavelength of 1064 nm, facilitating its active role in photothermal conversion.

Photothermal and photoacoustic performance

The fabrication of FPE involves the preparation of a composite material consisting of $Ti_3C_2T_x$ and PDMS on

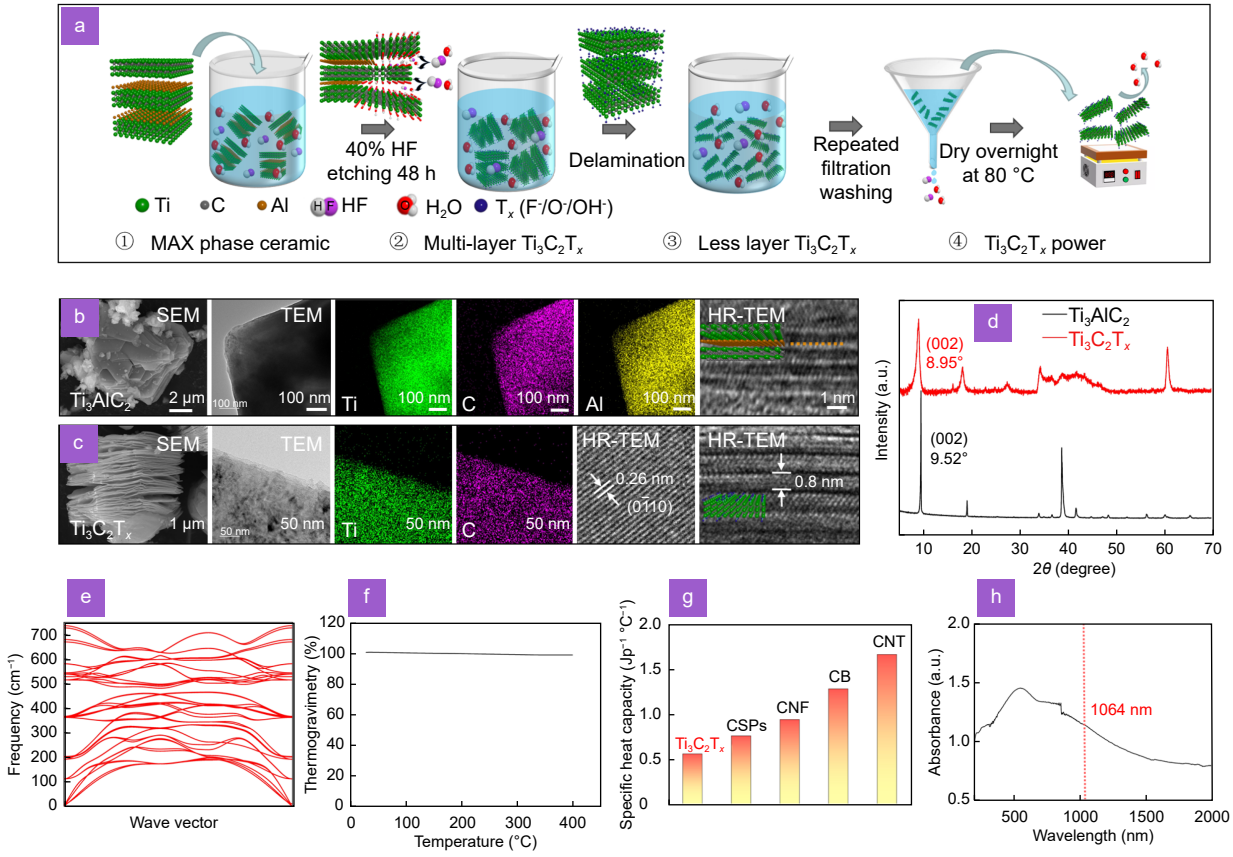

Fig. 2 | Characterizations of $Ti_3C_2T_x$. (**a**) Flow chart of preparation of $Ti_3C_2T_x$ by etching Ti_3AlC_2 with hydrofluoric acid. SEM and TEM image of Ti_3AlC_2 (**b**) and $Ti_3C_2T_x$ (**c**) with energy dispersive spectroscopy elemental mappings. (**d**) XRD patterns of Ti_3AlC_2 and $Ti_3C_2T_x$. (**e**) The phonon spectrum of $Ti_3C_2T_x$ through first-principles calculations. (**f**) The thermogravimetric curve of $Ti_3C_2T_x$. (**g**) Comparison of lattice specific heat capacities of different light-absorbing materials. CSPs: candle-soot carbon nanoparticles; CNF: carbon nanofibers; CB: carbon black; CNT: carbon nanotubes. (**h**) UV-visible-near-infrared-light absorption spectra of $Ti_3C_2T_x$.

the end face of a fiber-optic, where pulse laser induces a photothermal temperature field in $Ti_3C_2T_x$. The heat is conducted to PDMS, causing periodic expansion and contraction that generates ultrasound, with the photothermal effect of $Ti_3C_2T_x$ playing a crucial role in this process (Fig. 3(a)). Currently, $Ti_3C_2T_x$ is reported to exhibit a strong localized surface plasmon resonance (LSPR) effect across a wide spectrum due to its high density of metal-like free electrons and exceptional optoelectronic properties compared to other materials[31,32]. Owing to its excellent LSPR and layered structure, $Ti_3C_2T_x$ demonstrates strong photothermal conversion performance (Fig. 3(b)). Upon pulse lasers illumination, the $Ti_3C_2T_x$ plasmonic nanostructure absorbs pulse laser

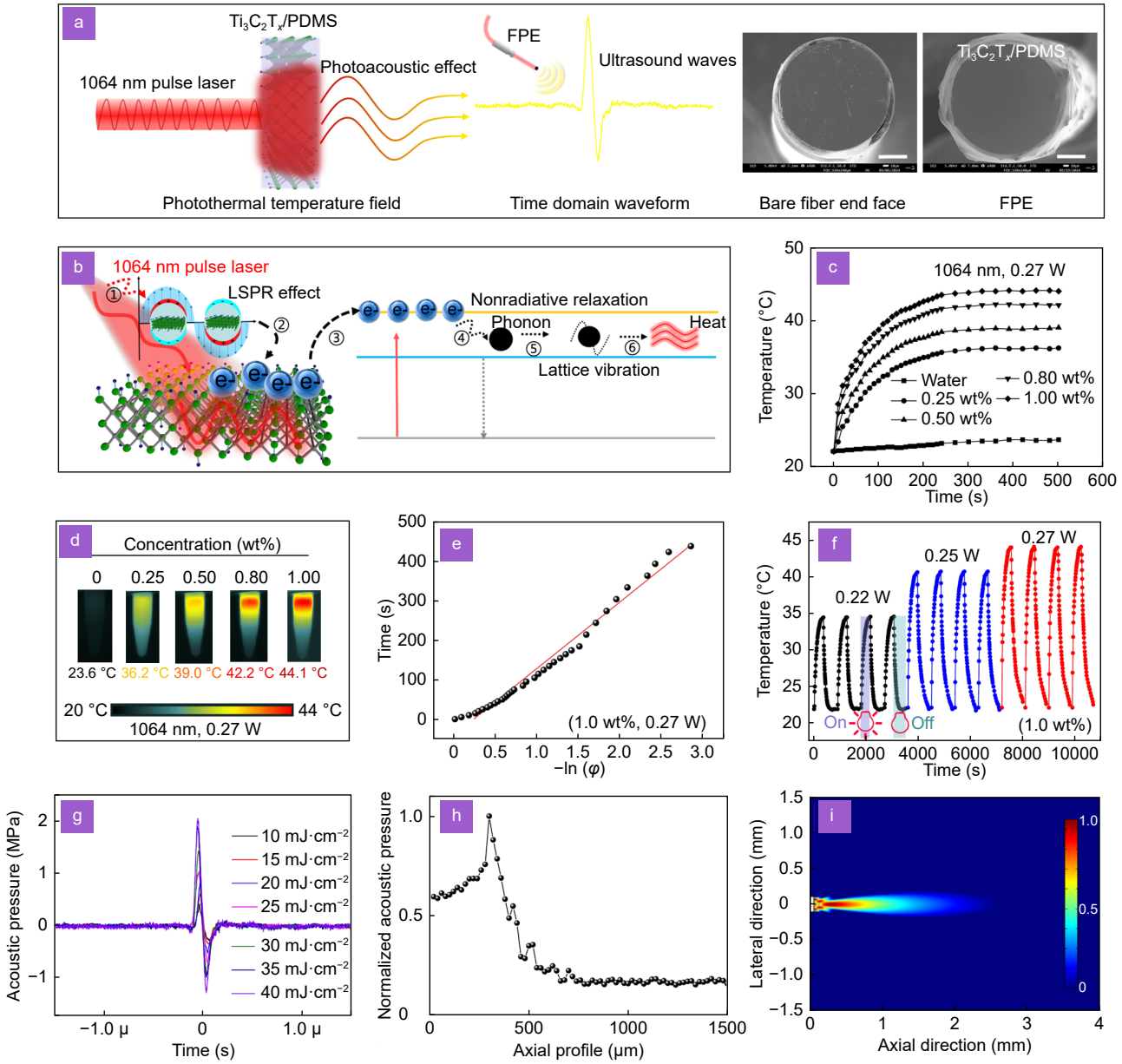

Fig. 3 | The photothermal and photoacoustic properties of $Ti_3C_2T_x$. (**a**) A pulse laser periodically regulates the photothermal temperature field of $Ti_3C_2T_x$ inducing PDMS to excite ultrasound waves, middle image: bare fiber end face, right image: FPE physical image. Scale bar: 50 μm. (**b**) Photothermal conversion mechanism of $Ti_3C_2T_x$, i: pulse laser radiation, ii: LSPR effect, iii: electron transitions, iv: electron-phonon coupling, v: lattice vibration, vi: lattice temperature rise. Temperature change curves (**c**) and infrared thermal images (**d**) of $Ti_3C_2T_x$ concentration: 1.0 wt%, 0.8 wt%, 0.5 wt%, 0.25 wt%, and pure water (1064 nm, 0.45 g, 0.27 W). (**e**) Fitting lines of time and −ln(*φ*) during the cooling process of $Ti_3C_2T_x$ (1.0 wt%, 0.27 W). (**f**) Temperature evolution of the $Ti_3C_2T_x$ in an aqueous dispersion under irradiation with a 1064 nm laser at 0.22 W, 0.25 W, and 0.27 W (1.0 wt%). (**g**) Time domain waveform of FPE excited ultrasound at different pulse laser energy densities. FPE axial acoustic field testing (**h**) and multiphysics simulation results (**i**).

energy from incident photons, inducing the generation of high-concentration, high-energy free electrons through electron transitions (i: pulse laser radiation → ii: LSPR effect → iii: electron transitions)[33]. The free electrons accumulate on the $Ti_3C_2T_x$ surface. The resulting photoexcitation of the LSPR is a global nonequilibrium process, where the dephasing and decay of the free electrons occur at ultrafast speeds[33,34]. To restore thermal equilibrium, the absorbed energy of electrons can be relaxed through either the radiative reemission of photons or the nonradiative generation of electron-hole pairs via Landau damping[35,36]. The energetic electrons (hot electrons) produced from nonradiative plasmon decay have a highly nonthermal distribution[37]. These hot electrons quickly interact with low-energy electrons. This electron-electron collision is an inelastic coulombic process that converts electron energy into heat. Simultaneously, low-energy electrons couple with the lattice through electron-phonon scattering processes (iv: electron-phonon coupling). This relaxation step leads to the thermalization of the lattice in the nanostructure (v: lattice vibration)[38]. Finally, the thermal energy inside the $Ti_3C_2T_x$ nanostructure is released to the surrounding PDMS through phonon-phonon collisions (vi: lattice temperature rise). With ultrasonic excitation, the electrons in the conduction band of the $Ti_3C_2T_x$ nanostructure eventually return to their ground states before photoexcitation. In the layered structure, the remaining pulse laser undergoes multiple internal reflections within the $Ti_3C_2T_x$ flakes, leading to more absorption and overall attenuation of the laser[39]. Consequently, the light energy absorbed by $Ti_3C_2T_x$ generates hot electrons through the LSPR effect. These hot electrons induce strong lattice vibration intensification through non-radiative transition-excited phonons, drastically increasing the lattice temperature of $Ti_3C_2T_x$ and inducing thermal expansion of PDMS.

The photothermal properties of $Ti_3C_2T_x$ were investigated using near-infrared (1064 nm) radiation. The photothermal conversion performance of $Ti_3C_2T_x$ was evaluated by recording temperature changes with thermal imaging photographs while irradiating with various concentrations (1.0 wt%, 0.8 wt%, 0.5 wt%, 0.25 wt%, and pure water) under a 1064 nm NIR laser (0.27 W) (Fig. 3(c, d)). The temperature of $Ti_3C_2T_x$ rapidly increased by 44 °C within 5 minutes due to its high efficiency in converting NIR light into thermal energy, demonstrating excellent photothermal effects for medical applications. The heating and cooling curves of $Ti_3C_2T_x$ demonstrate its excellent photothermal conversion property (Fig. 3(e), Fig. S2, and Section 2). In addition, the repeatable heating/cooling curves (on: laser radiation, off: laser stop radiation) indicate that $Ti_3C_2T_x$ possesses excellent photothermal stability, with no significant temperature change even after four irradiation cycles (Fig. 3(f)). This indicates that the continuous application of pulse laser to the FPE can consistently emit ultrasound. The ultrasound generated through the FPE is detected by a hydrophone and read out by an oscilloscope (Fig. S3). As shown in Fig. 3(g), the sound pressure intensity increases with the laser energy density. When the laser energy density is 10 mJ/cm^2, the peak-to-peak ultrasound intensity generated by the FPE is 0.7 MPa (positive peak 0.4 MPa, center frequency: 4 MHz). Additionally, the sound pressure intensity calculated using the photoacoustic theoretical model aligns with the experimental results (Supplementary information and Fig. S5). Low-intensity and broadband ultrasound is an emerging modality for neuromodulation, with the acoustic waves generated by the FPE enabling direct and spatially confined neural stimulation in vivo within a functional brain. However, the acoustic intensity is expected to attenuate when propagating through a medium. To experimentally characterize this attenuation with distance, we performed wavefront reconstruction for the lateral and axial sound field. All profiles were normalized to the peak amplitude of the signal for comparison. The lateral spatial resolution was determined as the full width at half maximum (FWHM) of the Gaussian fit to the lateral profiles (Fig. 1(b_2)). In contrast, the axial resolution, which is solely determined by the acoustic parameters, was measured using the FWHM of the enveloped axial line spread function (Fig. S6). We define the lateral and axial resolutions based on the FWHM in their respective directions[11,40–42]. The lateral and axial resolutions of the FPE were found to be 163.6 μm and 207 μm. The acoustic intensity attenuated by 50% at a distance of ~400 μm from the FPE underwater (Fig. 3(h)). The illustration in Fig. 3(i) shows the simulated distribution of the sound field energy for the transducer using COMSOL Multiphysics. The COMSOL simulation results indicate that the acoustic waves significantly decays along the axis. The miniature FPE, together with the rapid attenuation of photoacoustic intensity with distance, provides superior spatial confinement for neural stimulation. Performance summary of representative photoacoustic transducers, as shown in Table S2.

Photoacoustic stimulation activates mPFC neurons

The neuromodulatory effect of ultrasonic waves on neurons have been studied for the treatment of neurological diseases[7,43,44]. A key advantage of FPE over traditional ultrasound devices is that it emits ultrasound waves locally at the coated fiber tip, which allows high spatial precision reversible neural stimulation. To investigate the activation of mPFC neurons by photoacoustic stimulation, we utilized a TetTagging method to selectively express a cfos-promoter-inducible mCHERRY gene within the mPFC, as described previously[45]. This approach utilized a c-fos-dependent TetTagging system combined with an activity-responsive mCherry gene expression mechanism. In this system, mCherry expression was selectively triggered by neural activity, enabling the labeling of neuron ensembles activated by a stimulus in vivo. We employed two adeno-associated virus (AAV) viruses: one containing the cfos-TTA transgene and another containing the tet-operator promoter (TRE-tight) linked to an mCHERRY reading frame (Fig. 4(a)). The mice underwent simultaneous viral injections and fiber-optic photoacoustic emitter implantation in mPFC. Prior to photoacoustic stimulation, we initially suppressed the TetTag system using doxycycline (DOX) in their water. DOX prevented TTA from activating its target promoter, TRE-tight, located in the second AAV genome. Upon removal of DOX, neural activity could induce cfos promoter-linked TTA expression, subsequently activating mCHERRY expression (Fig. 4(a, b)). In our study, mice were kept on DOX water for 4 weeks, after which the DOX was removed to allow potential induction of the mCHERRY gene. Subsequently, the mice underwent either 0.8 MPa photoacoustic intensity stimulation or sham treatment, followed by administration of a sedative dose of DOX intraperitoneally. After another 4 weeks of DOX administration via drinking water, we observed widespread mCHERRY expression following photoacoustic stimulation (Fig. 4(c)), indicating neural activation in response to the stimulation.

Next, *in vivo* fiber photometry was employed to investigate the dynamics of mPFC neuron activation, enabling the recording of intracellular calcium transients in awake mice. To achieve this, we expressed the genetically encoded calcium indicator GCaMP6s in mPFC neurons via stereotaxic injection of rAAV-CaMKIIa-GCaMP6s into the mPFC of wild-type C57BL/6 mice (Fig. 4(d)). Concurrently, we implanted the fiber-optic photoacoustic emitter and the optic fiber. This approach enabled us to simultaneously administer photoacoustic stimulation and conduct fiber photometry recordings. We found that photoacoustic stimulation significantly activated mPFC neurons, eliciting remarkable calcium transients. Furthermore, we observed that photoacoustic stimulation of varying ultrasonic peak levels (0.4, 0.6, 0.8 MPa) induced calcium changes of differing intensities, showing a positive correlation. The neuronal excitation induced by photoacoustic stimulation peaked at approximately 4–6 seconds post-stimulation (Fig. 4(e-f)).

Photoacoustic stimulation of neurons in mPFC alleviates SDS-induced anxiety and social dysfunction

We next investigated whether photoacoustic stimulation of the mPFC could ameliorate neurofunctional deficits induced by SDS. We designed an experiment where the same cohort of mice underwent the following protocol (Fig. 5(a)). Initially, baseline activity and social behavior were assessed using the open-field test (OFT) and the 3 chamber test (before fight). Subsequently, the mice underwent a 1 hour SDS session to induce anxiety. OFT and 3 chamber test were used to assess the anxiety (after fight). After 1 hour of photoacoustic stimulation at 0.8 MPa, behavioral analysis was once again conducted using the OFT and the 3 chamber test to evaluate the efficacy of the photoacoustic stimulation treatment (after stim). After a 10 day interval, the animals underwent the same experimental procedures, with the exception of photoacoustic stimulation. Instead, fiber-optics were connected, but no stimulation was applied (after sham stim). This method effectively eliminated the influence of the initial experiment, enabling self-control.

The results showed that photoacoustic stimulation modulated both anxiety-like behavior and social interactions in mice. The OFT results indicated that while locomotor activity (measured as total distance traveled) and the duration in the center zone were decreased after SDS (Fig. 5(b-c)). The photoacoustic stimulation increased the time spent in the center zone of the arena, suggesting a reduction in anxiety (Fig. 5(d)). In the 3 chamber social interaction test, mice subjected to photoacoustic stimulation showed increased social engagement during the first session with a new mouse, highlighting the potential of photoacoustic stimulation in mPFC to enhance social behaviors in a novel environment (Fig. 5(f, g), Movie S1–S2). However, during the second session with a different novel mouse, this effect was not observed,

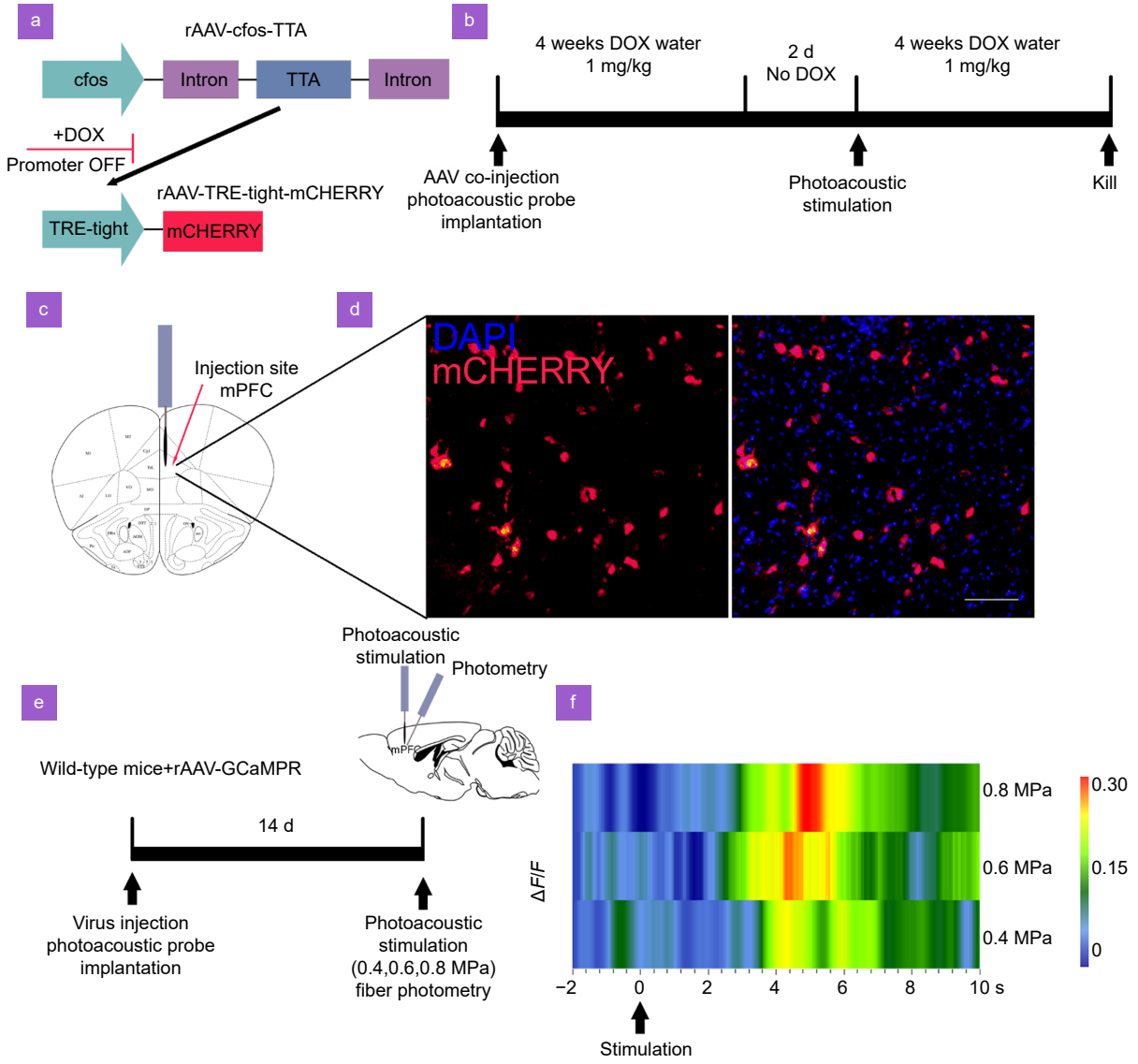

Fig. 4 | Photoacoustic stimulation activates mPFC neurons. (**a**) The AAV vectors. The first component contains the cfos promoter, responsible for driving the expression of the TTA protein. In the presence of DOX, TTA is unable to bind and activate its target promoter, TRE-tight, which is located in the second AAV. Upon removal of DOX, TTA becomes capable of activating mCHERRY expression. Importantly, this activation occurs exclusively in neurons where TTA expression has been induced by the cfos promoter, indicating neural activity. (**b**) Time line of the experimental procedure. Mice underwent a co-injection of AAV along with the implantation of the FPE. Subsequently, mice were administered DOX water (1 mg/mL) for four weeks, followed by a two-day period without DOX. This was followed by photoacoustic stimulation. Afterwards, mice received another four weeks of DOX in their drinking water. (**c**) Illustration showing the injection site of the AAV and FPE in the mPFC. (**d**) Immunofluorescent images displaying cfos expression in mPFC. DAPI (blue) stains the nuclei, and mCHERRY (red) indicates cfos expression. The left image shows cfos expression with photoacoustic stimulation, and the right image depicts the merged cfos and DAPI staining after stimulation. Scale bar: 100 μm. (**e**) Schematic of the fiber photometry setup for recording calcium signals in wild-type mice injected with rAAV-GCaMP. (f) Heatmap of calcium signal changes (Δ*F*/*F*) over time during photoacoustic stimulation (*n* = 4 mice).

indicating that the impact of the stimulation was specific to the initial social interaction.

Discussion

In this study, we developed a miniature, controllable sound intensity, and broadband FPE using $Ti_3C_2T_x$ and PDMS. The exceptional photothermal properties and a layered structure of $Ti_3C_2T_x$ can the photoacoustic emitter to excite broadband (−6 dB bandwidth: 162%) ultrasonic waves of different intensities. The FPE achieves lateral and axial resolutions of 163.6 μm and 207 μm, respectively, enabling high spatial precision reversible

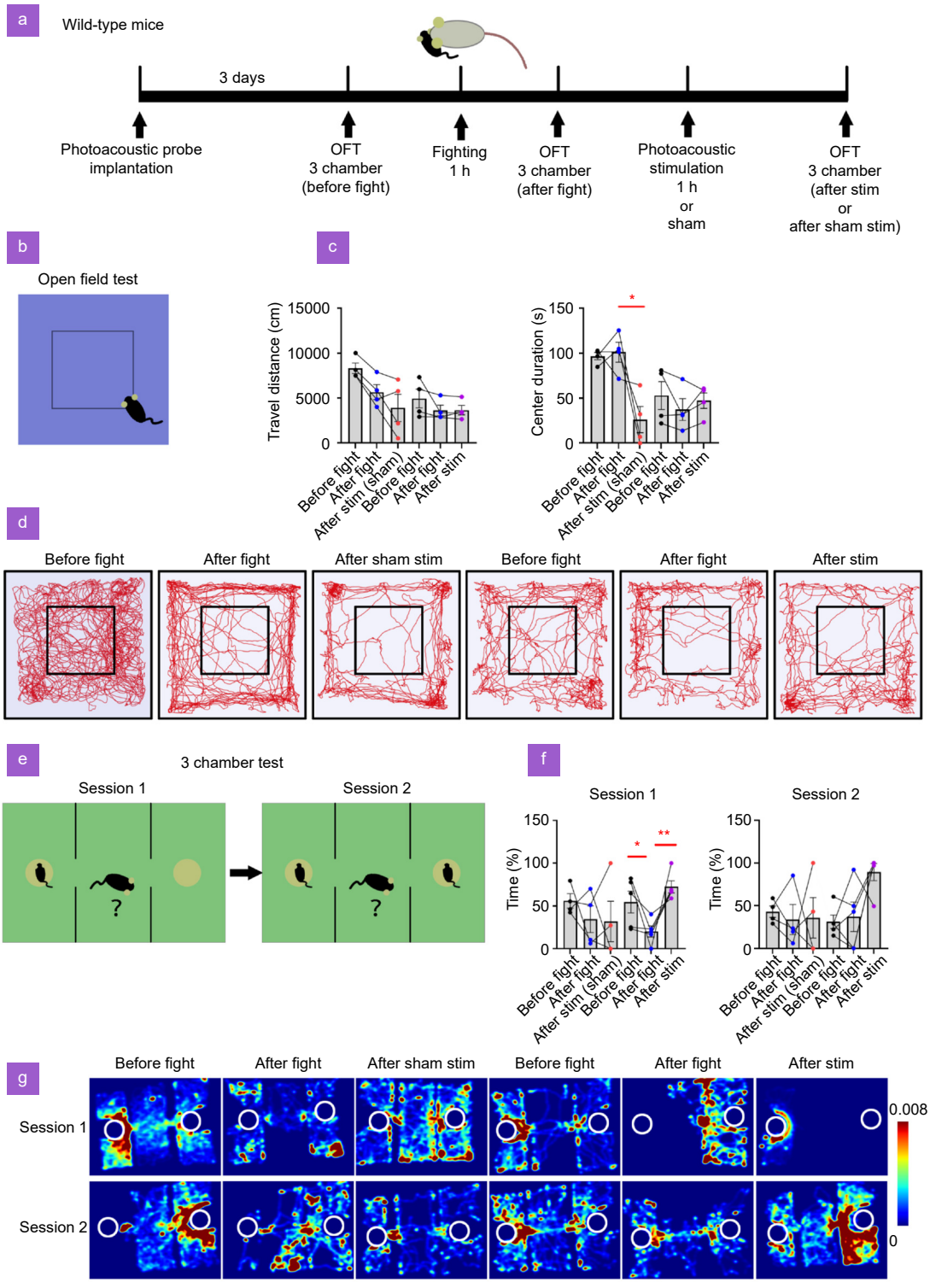

Fig. 5 | Photoacoustic stimulation of neurons in mPFC alleviates SDS-induced anxiety and social dysfunction. (**a**) Time line of the experimental procedure. Mice were implanted with a FPE. After 3 days, the mice underwent OFT and 3 chamber test to assess baseline behavior. Following a 1-hour SDS session, the anxiety was re-evaluated in the OFT and 3-chamber test. Subsequently, mice received either photoacoustic stimulation or sham stimulation for 1 hour before undergoing another OFT and 3 chamber test. (**b**) Diagram of the OFT setup and the central zone. (**c**) The total distance traveled and the time spent in the center zone of the OFT arena. (**d**) Representative trajectory plots from the OFT. (**e**) Diagram of the 3 chamber test. The diagrams represent session 1 and session 2. (**f**) Statistical analysis of the percentage of time spent with the left mouse in session 1 and the percentage of time spent with the right mouse in session 2. (**g**) Heatmaps of mouse movement trajectories. $^{*}p<0.05$, $^{**}p<0.01$.

neuromodulation. Our study demonstrated that the FPE stimulation of mPFC significantly alleviated anxiety behaviors and social deficits induced by acute SDS in mice across different individuals. Specifically, mice that received photoacoustic stimulation after acute SDS displayed less anxiety and more positive social behaviors in the open field test and 3-chamber test. Photoacoustic stimulation modulated the neural activity of the mPFC, restoring it to a more normal state and thereby reducing the behavioral abnormalities induced by acute stress. This effect may be achieved through several mechanisms. First, photoacoustic stimulation might restore the mPFC ability to regulate emotions and stress responses by modulating its neural activity. Dysfunction in the mPFC due to acute stress is likely a primary cause of anxiety and social avoidance, so restoring its normal function through photoacoustic stimulation can alleviate these symptoms. Additionally, acute stress may disrupt the functional connectivity between the mPFC and other emotion-related brain regions, such as the amygdala and hippocampus[46]. By modulating mPFC activity, photoacoustic stimulation may help restore these functional connections, thereby improving overall emotional regulation. Lastly, acute stress activates the stress, immune, and oxidative system, potentially creating a state of mutual activation that leads to persistent behavioral and biochemical changes[47]. By directly modulating mPFC activity, photoacoustic stimulation might interrupt this vicious cycle, restoring the brain to its normal physiological state.

In summary, FPE provides a high spatial precision and reversible neural stimulation method applicable to neurological research in specific brain regions. This study highlights the potential of FPE in addressing stress-related psychiatric disorders. Its fabrication flexibility and enhanced electromagnetic compatibility facilitate clinical applications, including Parkinson's disease, epilepsy, chronic pain, and mood disorders.

References

1. Hou XD, Jing JN, Jiang YZ et al. Nanobubble-actuated ultrasound neuromodulation for selectively shaping behavior in mice. *Nat Commun* **15**, 2253 (2024).
2. Piech DK, Johnson BC, Shen K et al. A wireless millimetre-scale implantable neural stimulator with ultrasonically powered bidirectional communication. *Nat Biomed Eng* **4**, 207–222 (2020).
3. Shi LL, Jiang Y, Fernandez FR et al. Non-genetic photoacoustic stimulation of single neurons by a tapered fiber optoacoustic emitter. *Light Sci Appl* **10**, 143 (2021).
4. Cotero V, Graf J, Miwa H et al. Stimulation of the hepatoportal nerve plexus with focused ultrasound restores glucose homoeostasis in diabetic mice, rats and swine. *Nat Biomed Eng* **6**, 683–705 (2022).
5. Leinenga G, Langton C, Nisbet R et al. Ultrasound treatment of neurological diseases-current and emerging applications. *Nat Rev Neurol* **12**, 161–174 (2016).
6. Yoon CW, Lee NS, Koo KM et al. Investigation of ultrasound-mediated intracellular Ca^{2+} oscillations in HIT-T15 pancreatic β-cell Line. *Cells* **9**, 1129 (2020).
7. Hou JF, Nayeem MOG, Caplan KA et al. An implantable piezoelectric ultrasound stimulator (ImPULS) for deep brain activation. *Nat Commun* **15**, 4601 (2024).
8. Sato T, Shapiro MG, Tsao DY. Ultrasonic neuromodulation causes widespread cortical activation via an indirect auditory mechanism. *Neuron* **98**, 1031–1041.e5 (2018).
9. Guo HS, Hamilton M, Offutt SJ et al. Ultrasound produces extensive brain activation via a cochlear pathway. *Neuron* **98**, 1020–1030.e4 (2018).
10. Krauss JK, Lipsman N, Aziz T et al. Technology of deep brain stimulation: current status and future directions. *Nat Rev Neurol* **17**, 75–87 (2021).
11. Chen G, Yu FY, Shi LL et al. High-precision photoacoustic neural modulation uses a non-thermal mechanism. *Adv Sci* **11**, 2403205 (2024).
12. Du ZY, Chen G, Li YM et al. Photoacoustic: A versatile non-genetic method for high-precision neuromodulation. *Acc Chem Res* **57**, 1595–1607 (2024).
13. Seo D, Neely RM, Shen K et al. Wireless recording in the peripheral nervous system with ultrasonic neural dust. *Neuron* **91**, 529–539 (2016).
14. Lee T, Baac HW, Li QC et al. Efficient photoacoustic conversion in optical nanomaterials and composites. *Adv Opt Mater* **6**, 1800491 (2018).
15. Li JP, Yang Y, Chen ZY et al. Self-healing: a new skill unlocked for ultrasound transducer. *Nano Energy* **68**, 104348 (2020).
16. Ma TG, Wang HZ, Guo LJ. OptoGPT: A foundation model for inverse design in optical multilayer thin film structures. *Opto-Electron Adv* **7**, 240062 (2024).
17. Liu HH, Hu DJJ, Sun QZ et al. Specialty optical fibers for advanced sensing applications. *Opto-Electron Sci* **2**, 220025 (2023).
18. Mu MD, Geng HY, Rong KL et al. A limbic circuitry involved in emotional stress-induced grooming. *Nat Commun* **11**, 2261 (2020).
19. Karatsoreos IN, McEwen BS. Psychobiological allostasis: resistance, resilience and vulnerability. *Trends Cogn Sci* **15**, 576–584 (2011).
20. Kotlęga D, Gołąb-Janowska M, Masztalewicz M et al. The emotional stress and risk of ischemic stroke. *Neurol Neurochir Pol* **50**, 265–270 (2016).
21. Gilboa T. Emotional stress-induced seizures: another reflex epilepsy. *Epilepsia* **53**, e29–e32 (2012).
22. Ochsner KN, Silvers JA, Buhle JT. Functional imaging studies of emotion regulation: a synthetic review and evolving model of the cognitive control of emotion. *Ann N Y Acad Sci* **1251**, E1–E24 (2012).
23. Hermans EJ, Henckens MJAG, Joëls M et al. Dynamic adaptation of large-scale brain networks in response to acute stressors. *Trends Neurosci* **37**, 304–314 (2014).
24. van Oort J, Tendolkar I, Hermans EJ et al. How the brain

connects in response to acute stress: A review at the human brain systems level. *Neurosci Biobehav Rev* **83**, 281–297 (2017).
25. Somerville LH, Wagner DD, Wig GS et al. Interactions between transient and sustained neural signals support the generation and regulation of anxious emotion. *Cereb Cortex* **23**, 49–60 (2013).
26. Sinha R, Lacadie CM, Constable RT et al. Dynamic neural activity during stress signals resilient coping. *Proc Natl Acad Sci USA* **113**, 8837–8842 (2016).
27. Kalinichenko LS, Kornhuber J, Müller CP. Individual differences in inflammatory and oxidative mechanisms of stress-related mood disorders. *Front Neuroendocrin* **55**, 100783 (2019).
28. Gao JH, Zhang L, Zhu JF et al. Prefrontal cortex hemodynamics and functional connectivity changes during performance working memory tasks in older adults with sleep disorders. *Brain Sci* **13**, 497 (2023).
29. Liu TT, Qi CX, Bai WW et al. Behavioral state-dependent oscillatory activity in prefrontal cortex induced by chronic social defeat stress. *Front Neurosci* **16**, 885432 (2022).
30. Chen JJ, Jin QQ, Li YB et al. Molten salt‐shielded synthesis (MS^3) of MXenes in sir. *Energy Environ Mater* **6**, e12328 (2023).
31. Lu HZ, Wang JH, Li HM et al. Efficient photothermal conversion of MXenes and their application in biomedicine. *Mater Chem Front* **7**, 4372–4399 (2023).
32. Sayed M, Yu JG, Liu G et al. Non-noble plasmonic metal-based photocatalysts. *Chem Rev* **122**, 10484–10537 (2022).
33. Cui XM, Ruan QF, Zhuo XL et al. Photothermal nanomaterials: a powerful light-to-heat converter. *Chem Rev* **123**, 6891–6952 (2023).
34. Brongersma ML, Halas NJ, Nordlander P. Plasmon-induced hot carrier science and technology. *Nat Nanotechnol* **10**, 25–34 (2015).
35. Liu JG, Zhang H, Link S et al. Relaxation of Plasmon-induced hot carriers. *ACS Photonics* **5**, 2584–2595 (2018).
36. Bernardi M, Mustafa J, Neaton JB et al. Theory and computation of hot carriers generated by surface Plasmon polaritons in noble metals. *Nat Commun* **6**, 7044 (2015).
37. Linic S, Aslam U, Boerigter C et al. Photochemical transformations on plasmonic metal nanoparticles. *Nat Mater* **14**, 567–576 (2015).
38. Baffou G, Quidant R. Thermo-plasmonics: using metallic nanostructures as Nano-sources of heat. *Laser Photonics Rev* **7**, 171–187 (2013).
39. Shahzad F, Alhabeb M, Hatter CB et al. Electromagnetic interference shielding with 2D transition metal carbides (MXenes). *Science* **353**, 1137–1140 (2016).
40. Xing WX, Wang LD, Maslov K et al. Integrated optical- and acoustic-resolution photoacoustic microscopy based on an optical fiber bundle. *Opt Lett* **38**, 52–54 (2013).
41. Ansari R, Zhang EZ, Desjardins AE et al. All-optical forward-viewing photoacoustic probe for high-resolution 3D endoscopy. *Light Sci Appl* **7**, 75 (2018).
42. Du XY, Li JP, Niu GD et al. Lead halide perovskite for efficient optoacoustic conversion and application toward high-resolution ultrasound imaging. *Nat Commun* **12**, 3348 (2021).
43. Yu K, Niu XD, Krook-Magnuson EK et al. Intrinsic functional neuron-type selectivity of transcranial focused ultrasound neuromodulation. *Nat Commun* **12**, 2519 (2021).
44. Murphy KR, Farrell JS, Bendig J et al. Optimized ultrasound neuromodulation for non-invasive control of behavior and physiology. *Neuron* **112**, 3252–3266.e5 (2024).
45. Zhang Z, Ferretti V, Güntan İ et al. Neuronal ensembles sufficient for recovery sleep and the sedative actions of α_2 adrenergic agonists. *Nat Neurosci* **18**, 553–561 (2015).
46. Kim J, Kang S, Choi TY et al. Metabotropic glutamate receptor 5 in amygdala target neurons regulates susceptibility to chronic social stress. *Biol Psychiatry* **92**, 104–115 (2022).
47. Cattane N, Vernon AC, Borsini A et al. Preclinical animal models of mental illnesses to translate findings from the bench to the bedside: molecular brain mechanisms and peripheral biomarkers associated to early life stress or immune challenges. *Eur Neuropsychopharmacol* **58**, 55–79 (2022).

Acknowledgements

This work was supported by the National Nature Science Foundation of China (Grant Number: U24A20306, 12102140, 6227031087, 62035006, and 6207030117).

Author contributions

Z.L. and X.L. conceived the idea. J.L., Z.X., and S.Y. designed and manufactured the $Ti_3C_2T_x$/PDMS fiber-optic photoacoustic emitter. X.L. Z.L. and S.G. designed and completed biomedical experiments. Z.X. and Y.W. performed photothermal and photoacoustic experiments. M.S. and S.Y. performed the theoretical calculation. H.J. performed analytical simulations. X.F., X.G., Y.W., and T.G. participated in the project discussion. All the authors contributed to the paper writing. Z.L. and X.L. provided overall guidance and supervised the study. We also thank the Prof. Yi Guo and Prof. Xue Yang of Analytical and Testing Center of Wuhan University of Technology.

Competing interests

The authors declare no competing financial interests.

Ethical statement

All experiments were performed according to Guidelines for Animal Experimentation of the Animal Experimentation Ethics Committee of the Tongji Hospital affiliated with Huazhong University of Science and Technology. Ethical approval for the study was granted (Approval No. TJH-202307029).

Supplementary information

Supplementary information for this paper is available at https://doi.org/10.29026/oes.2025.240034